Hindawi
Shock and Vibration
Volume 2024, Article ID 5868224, 12 pages
https://doi.org/10.1155/2024/5868224

Research Article

Researching the Influence of Preload on Vibration Characteristics in the Ballistic Recorder Vibration Damping System

Wencan Jiang,[1] **Yonggang Lu**,[1] **and Jianyu Zhao**[2]

[1]*Institute of Systems Engineering, China Academy of Engineering Physics, Mianyang 621999, China*
[2]*Sichuan Widdenton Construction Co., Ltd., Mianyang 621053, China*

Correspondence should be addressed to Yonggang Lu; lygcaep@263.net

Received 17 October 2023; Revised 16 February 2024; Accepted 19 February 2024; Published 30 April 2024

Academic Editor: Vasudevan Rajamohan

In this study, the vibration characteristics of a bullet-loaded recorder's vibration damping system under various preload conditions are investigated through theoretical analysis, numerical simulations, and experimental verification. The findings indicate that the inclusion of a polyurethane elastomer vibration damping buffer layer between the cartridge and the recorder, along with the application of a specific preload, significantly reduces the amplitude of vibration acceleration transmitted to the recorder's interior. This, in turn, enhances the overload resistance of the cartridge's internal circuit. Numerical simulation results and theoretical analysis suggest that increasing the preload on the buffer material between the elastomer and the recorder reduces both the frequency ratio and damping ratio of the damping system. This reduction further decreases the amplitude of vibration transmitted to the recorder. However, excessively high preload generates substantial compressive stress within the recorder under static conditions, intensifying during the projectile's accelerated movement. As a consequence, deformation and damage occur to the internal circuitry. Therefore, ensuring that the recorder possesses the structural strength necessary to withstand increased preload is crucial. This balancing act improves the recorder's resistance to shock, vibration, and overload, while also preventing excessive stress-induced damage.

1. Introduction

In high-speed or ultrahigh-speed weapon systems, achieving rapid muzzle velocity for the projectile, even over short distances, is crucial. However, rapid acceleration during launch exposes the system to prolonged periods of intense overload impact. This overload shock consistently correlates with high acceleration levels and shock-induced vibrations at high frequencies. Therefore, optimizing the internal circuitry's resilience within the weapon system during high-overload launch conditions carries profound significance.

A ballistic recorder is a data acquisition device used for collecting and recording bullet-related information to support research. When an external stress wave enters a material with a low acoustic impedance from one with a high acoustic impedance, it reflects and reduces the amplitude of the stress wave. Thus, employing a hard-soft-hard-soft structure from the outermost to the innermost layer achieves vibration protection for the internal circuit system. This involves using hard metal materials, soft materials, hard metal materials, and soft materials for vibration damping from exterior to interior, effectively reducing stress wave amplitudes. Extensive research has been conducted on this protective structure [1–3]. Cheng et al. [1] establish a simplified model for the dynamics of the protective system. Previous research findings demonstrate that enhancing the inherent frequency of the protective system is advantageous when high-impact load frequency components are primarily concentrated in the low-frequency range. Measures such as reducing the mass of circuit components and appropriately increasing support stiffness prove beneficial. Xu et al. [2] find

that decreasing values of the nonlinear modulus of elasticity, elastic constants of low strain rate Maxwell units, relaxation time of high strain rate Maxwell units, and material density improve the potting material's vibration damping and protection properties.

Soft materials, such as polyurethane, rubber, epoxy resins, or silicone gels, are commonly used as potting materials. These materials demonstrate hyperelastic properties with a lower speed of sound, resulting in lower acoustic impedance compared to metals. While soft materials can absorb shock through their own deformation during stress wave propagation, reducing peak loads, they present challenges. Deformation of the cushioning material might create a gap between the inner metal structure and the cushioning material, potentially amplifying vibration output to the inner protective structure during high-frequency overload impacts [2]. This scenario is unfavorable for improving the system's protective performance, especially when projectiles induce violent oscillations in the complex fluid environment upon leaving the muzzle [4–7]. Enhancing the stiffness of the vibration isolator, particularly when the input frequency is lower than the system's intrinsic frequency, could reduce overload transfer to inner circuit components [1]. Previous research [8–11] suggests that precompressing the buffer material enhances the stiffness of the vibration isolator. Therefore, designing a specific interference assembly between the buffer material and the inner circuit assembly, along with applying precompression force on the buffer material through an interference fit, is considered to enhance its stiffness. However, further investigation is necessary to determine whether this interference fit could improve the system's protection performance under high-overload impacts. Additionally, understanding its vibration damping mechanism is crucial.

Rubber materials have traditionally been used for structural vibration damping [12–15], and extensive research has focused on using rubber as the outer protective material for ballistic recorders. Remarkably, the existing literature has largely overlooked the application of a specific precompressive force between the recorder and the cushioning material. Assembly clearances can cause significant relative motion between the ballistic recorder and the protective material. This can potentially create substantial gaps, especially in high-overload launch environments. If not addressed, this relative motion could cause severe internal oscillations of the recorder within the cushioning material during launch or after leaving the muzzle, increasing the risk of recorder damage and failure. Previous studies have confirmed the significant damping properties of polyurethane elastomers in mitigating impact and vibrations. This paper suggests applying precompressive forces between the recorder and the cushioning material to counteract potential gaps due to relative motion in high-overload environments. The study explores how varying precompressive forces impact overload resistance and system vibration reduction performance using theoretical frameworks and numerical simulations. The research aims to provide valuable insights for improving overload resistance and vibration protection in high-speed or ultrahigh-speed launch systems.

2. Ballistic Recorder Protection System Design

The ballistic recorder consists of four primary sections in Figure 1: the head section, the power section, the telemetry section, and the antenna section. The head section includes the ballistic recorder itself, the outer protective structure, and the connecting threads that join these components. Both the power section and the head have threaded shells for applying preload, with thread limits set to meet interference assembly requirements. The outer protective structure is constructed using polyurethane elastomer potting material. The volume of the polyurethane elastomer is carefully designed. Potting is executed in accordance with the designated interference parameters. After the curing process is completed, preload is applied. Applying torque via the threaded connection applies force to the protective component, subsequently applying preload to the recorder.

3. Numerical Simulation Calculation Model and Parameters

The shell structure is simplified, and the simplified model is displayed in Figure 2. The shell and outer protection are designed with an interference fit. Preload is applied through these surfaces. The numerical simulation model employs an interference fit on the end face to apply preload force to the internal recorder component.

Overfitting is applied using the keyword ∗CONTACT_SURFACE_TO_SURFACE_INTERFERENCE, combined with ∗CONTROL_DYNAMIC_RELAXATION for stress relaxation. The relaxation time is set at 2 milliseconds. Acceleration loading is applied to the end face, and the loading curve is determined using experimentally measured data, as shown in Figure 3. The maximum acceleration experienced by the projectile is 18074.2 g, with the entire overload duration lasting 14.5 milliseconds. Here, "g" represents gravity acceleration with a value of 9.8 m/s^2, as indicated in the following text. The acceleration profile is not perfectly smooth. It exhibits several sawtooth patterns within the acceleration section. The sudden increase in projectile acceleration upon exiting the gunnel may have been attributed to the rapid reduction of friction upon exit, along with significant velocity fluctuations resulting from the free expansion of propellant gas and the rapid decrease in air resistance.

Numerical simulation calculations are carried out using a three-dimensional 1/2 model with a mesh size of 1 mm. All structures are analyzed using the Lagrange algorithm. The shell material is constructed from high-strength alloy steel, specifically G50 steel. Material numerical simulations are conducted using both the Johnson–Cook eigenstructural model and the Gruneisen equation of state. In the Johnson–Cook eigenstructural model, the yield stress is represented by the following equation (16):

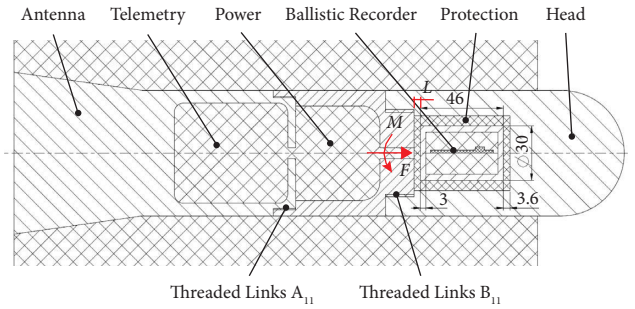

Figure 1: Structural design of ballistic recorder.

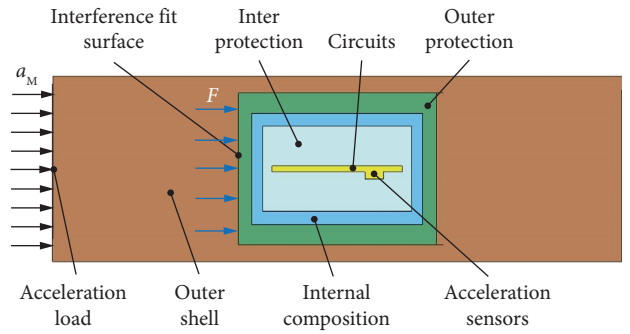

Figure 2: Computational model for numerical simulation.

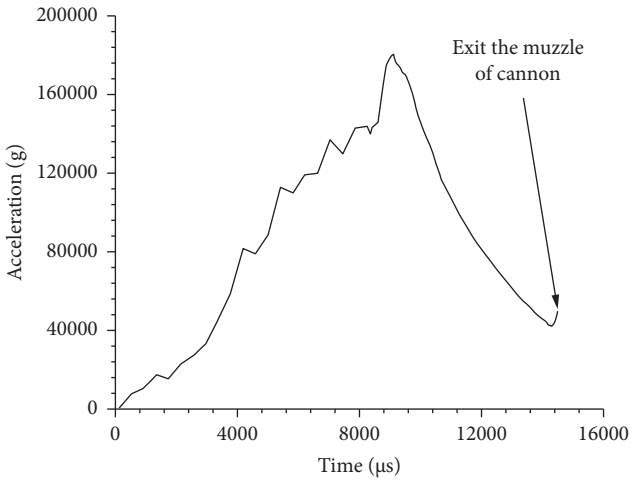

Figure 3: Bore overload curves measured in artillery tests.

$$\sigma_y = \left(A + B\bar{\varepsilon}^{p^n}\right)\left(1 + cln\dot{\varepsilon}^*\right)\left(1 + mln\frac{T - T_{\text{room}}}{T_{\text{melt}} - T_{\text{room}}}\right). \quad (1)$$

In this equation, A represents the initial yield stress of the material under the reference strain rate and reference temperature, denoted as T_{room} at that time. Additionally, B and n are the strain-hardening modulus and hardening index of the material under the reference strain rate and reference temperature, respectively. C stands for the strain rate strengthening parameter of the material, while ε represents the effective plastic strain, and m indicates the thermal softening parameter of the material.

The Gruneisen equation of state is used to determine the pressure of the material in compression, as described in [17]:

$$p = \frac{\rho_0 C^2 \mu\left[1 + (1 - (\gamma_0/2))\mu - (a/2)\mu^2\right]}{\left[1 - (S_1 - 1)\mu - S_2\left(\mu^2/\mu - 1\right) - S_3\left(\mu^3/(\mu + 1)^2\right)\right]} + (\gamma_0 + a\mu)E. \quad (2)$$

In this context, C, S_1, S_2, and S_3 are all determined by fitting the particle velocity profile v_s-v_p. γ_0 is used to represent the Gruneisen coefficient, while the coefficient a in equation (2) is a dimensionless parameter, and γ_1 is the first-order volume correction term.

$$\mu = \frac{\rho}{\rho_0} - 1. \quad (3)$$

E represents the internal energy. The material parameters for G50 steel are presented in Table 1.

The outer protection is constructed using polyurethane elastomer potting material. To consider the effect of strain rate, this study utilized both the Johnson–Cook model and the Gruneisen equation of state. In this research, a Hopkinson rod test is conducted to subject the polyurethane elastomer material to strain rate loading at different rates ($500s^{-1}$, $2000s^{-1}$, and $5000s^{-1}$) to derive the parameters of the Johnson–Cook eigenmodel (A, B, n, c, and m). Figure 4 depicts the true strain-stress curves of polyurethane elastomers obtained from tests at various strain rates.

Fitting the parameters involves the conversion of the true strain-stress curve into a true stress-plastic strain curve. The corresponding parameters are obtained through parameter fitting. In this study, the parameter n in the Johnson–Cook model is set to 0 since the impact of thermal softening due to temperature is not considered. The selection of other parameters is based on previous literature sources [19]. The associated parameters are detailed in Table 2.

The inner structure, fabricated from titanium alloy, is also represented using both the Johnson–Cook intrinsic model and the Gruneisen equation of state. The associated parameters are detailed in Table 3.

The circuit board, the accelerometer chip, and the inner potting material are all made from epoxy resin. They are parameterized using the plastic-kinematic intrinsic model. The yield stress is represented as σ_y [17].

$$\sigma_y = \sigma_0 + \beta E_h \varepsilon_{\text{eff}}^p, \quad (4)$$

where σ_0 represents the initial yield strength, E_h represents the hardening modulus, and $\varepsilon_{\text{eff}}^p$ is the effective plastic strain, The hardening modulus is defined as follows:

$$E_h = \frac{E_t E}{E - E_t}, \quad (5)$$

where E represents the elastic model, E_t represents the tangent modulus, and p represents the pressure. The associated parameters are detailed in Table 4.

In the context of the contact algorithm, the inner epoxy potting material, the circuit, and the accelerometer chip are designated as binding constraints. One-sided erosion contact is applied to other materials.

Table 1: Shell material model and parameters [18].

Material	Steel
MAT_JOHNSON-COOK	
G (GPa)	81.8
A (MPa)	1445
B (MPa)	1326
C	0.005
m	1.12
n	0.365
T_{room} (K)	393
T_{melt} (K)	1763
EOS_GRUEISEN	
ρ (g/cm^3)	7.75
C_0 (m/s)	4530
S (m/s)	1.49
C_v (GPa/K)	525
Γ	1.23

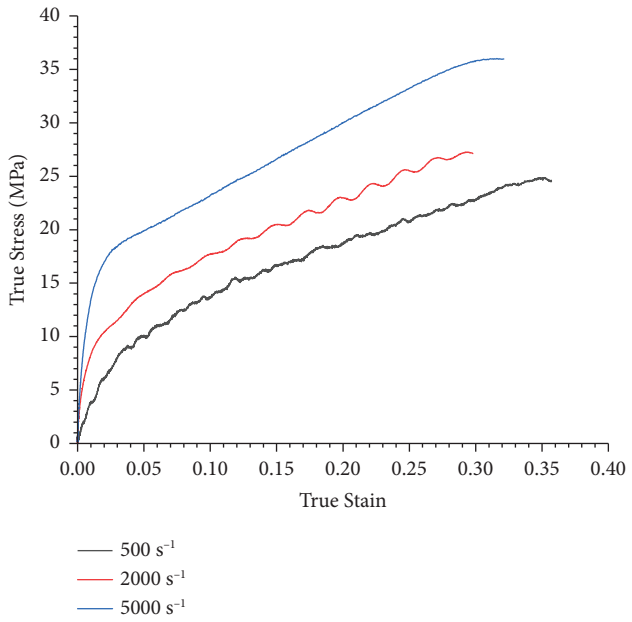

Figure 4: True strain-stress curves of polyurethane elastomers at different strain rates.

Table 2: Polyurethane elastomer material model and parameters.

Material	Polyurethane elastomers
A (MPa)	4.04389
B (MPa)	38.73164
C	0.50641
m	0.134875
n	0.0
T_{room} (K)	294
T_{melt} (K)	445
ρ (g/cm^3)	1.1
C_0 (m/s)	4695
S (m/s)	1.147
C_v (GPa/K)	1256
Γ	2.04

Table 3: Material modeling and parameters of titanium alloys [20].

Material	Titanium alloys
MAT_JOHNSON-COOK	
G (MPa)	44.0
A (MPa)	1098
B (MPa)	1092
C	0.014
m	1.1
n	0.93
T_{room} (K)	294
T_{melt} (K)	1941
EOS_GRUEISEN	
ρ (g/cm^3)	4.51
C_0 (m/s)	2486
S_1	1.577
C_v (GPa/K)	528
Γ	1.55

Table 4: Epoxy resin material model and parameters.

Material	Epoxy resin
MAT_PLASTIC-KINEMATIC	
ρ (g/cm^3)	1.186
G (GPa)	1.45
σ_Y (MPa)	40.0
E (GPa)	11.26
ETAN (GPa)	4.08

4. Results and Discussion

4.1. Response Modeling of Protection Systems under Overload. The ballistic recorder protection system is simplified to the model depicted in Figure 5. Assuming that the deformation arising from the outer protection took place within the elastic deformation stage, the differential equation of motion, as per Newton's laws of motion, read as follows:

$$\begin{aligned} M\ddot{x}_M &= Ma_M - F_{1B} - F_{2B}, \\ m\ddot{x}_m &= F_{1A} + F_{2A}, \\ F_{1A} &= F_{1B} = k(x_M - x_m), \\ F_{2A} &= F_{2B} = c(\dot{x}_M - \dot{x}_m), \end{aligned} \tag{6}$$

where M represents the mass of the ballistic recorder protection system, excluding the recorder. m is the mass of the recorder. a_M is the acceleration of the ballistic recorder protection system. F_{1A} and F_{1B} are the spring force acting on the recorder and system. k is the stiffness coefficient of the system. F_{2A} and F_{2B} are the damping forces acting on the recorder and system. c is the damping coefficient of the system. $\dot{x}_M$ and $\dot{x}_m$ are the first-order partial derivative of the protection system and recorder displacement. $\ddot{x}_M$ and $\ddot{x}_m$ are the second-order partial derivative of the protection system and recorder displacement.

The Laplace transform of the equation is obtained:

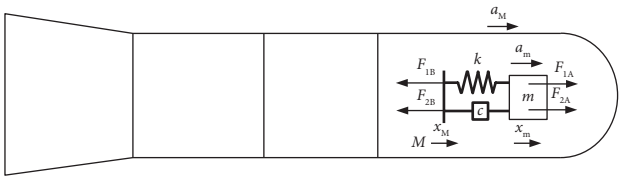

Figure 5: Physical model diagram of the ballistic recorder protection system.

$$\frac{X_m}{A_m} = \frac{cs + k}{s^2\left[ms^2 + (1 + m/M)(cs + k)\right]}. \tag{7}$$

Given that "a_m" represents "d^2x_m/dt^2," it is expressed as "$A_m = s^2X_m$." In the design of the ballistic recorder at that time, M is considerably larger than m, allowing for the simplification of the above equation to:

$$\frac{A_m}{A_M} = \frac{cs + k}{ms^2 + cs + p} = \frac{c/ms + p/m}{s^2 + c/ms + p/m} = \frac{2\zeta\omega_n s + \omega_n^2}{s^2 + 2\zeta\omega_n s + \omega_n^2}. \tag{8}$$

In this context, ω_n denotes the system's intrinsic frequency in radians per second, while ζ represents the dimensionless damping ratio of the system. When the input signal is sinusoidal ($s = j\omega$), the transfer function of the system could be obtained as follows:

$$\left|\frac{A_m(j\omega)}{A_M(j\omega)}\right| = \frac{\sqrt{1 + 4\zeta^2(\omega/\omega_n)^2}}{\sqrt{\left[1 - (\omega/\omega_n)^2\right]^2 + 4\zeta^2(\omega/\omega_n)^2}}. \tag{9}$$

Demonstrating the correlation between the system's transfer function and the damping ratio and frequency ratio, the fitted variation curve is presented in Figure 6.

The analysis yields the following conclusions when the input is a sinusoidal function:

When ω/ω_n is less than 1, the transfer function gradually increases as ω/ω_n increases. Therefore, for protection systems with ω/ω_n less than 1, increasing the intrinsic frequency ω_n of the protection system could reduce the overload output to the recorder.

When ω/ω_n is greater than 1, the output transfer function gradually decreases as ω/ω_n increased. For a protection system with ω/ω_n greater than 1, reducing the intrinsic frequency ω_n of the protection system could lower the overload output to the recorder.

Increasing the damping ratio results in a gradual decrease in the maximum magnitude of the output. Therefore, enhancing the damping of the outer protective material could reduce the overload on the recorder.

For ω/ω_n greater than 1, when ω/ω_n exceeds a certain value, the change in amplitude drop became weaker as the value of ω/ω_n increases. A similar situation is applied to the damping ratio; when it exceeds a certain value, further increases in the damping ratio lead to a weaker change in amplitude drop. Hence, appropriate preload is beneficial for vibration damping of the recorder, but excessive preload may result in damage to the recorder.

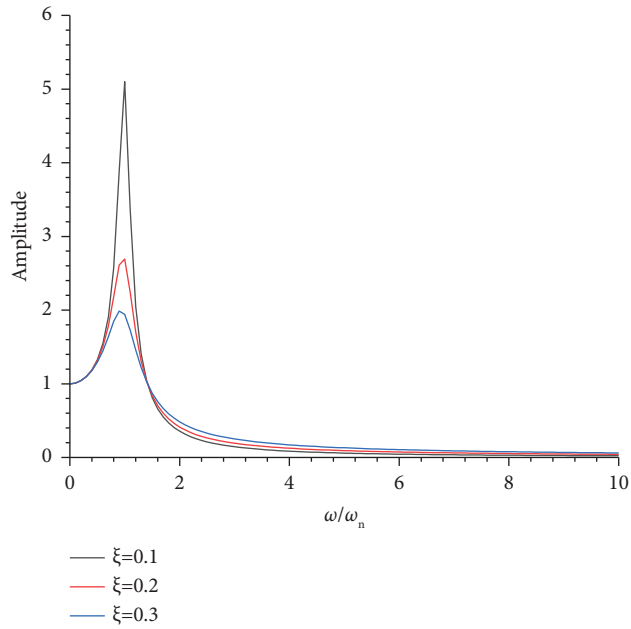

Figure 6: Transfer function amplitude versus frequency ratio and damping ratio curves.

The stiffness coefficient of the polyurethane elastomer changes when the model underwent predeformation. The relationship between the quasistatic force F_0 and the precompression displacement u_0 is as follows [10]:

$$F_0 = \frac{3\pi}{4}\frac{\mu_1 D^2\mu_0}{(H - \mu_0)^2}\left[1 + \frac{D^2(2H - \mu_0)}{16H^2(H - \mu_0)}\right]. \tag{10}$$

Thus, the quasistatic stiffness factor can be obtained as follows:

$$k_0 = \frac{dF_0}{du_0} = \frac{3\pi}{4}\frac{\mu_1 D^2\mu_0}{(H - \mu_0)^2}\left[1 + \frac{D^2}{8H(H - \mu_0)}\right]. \tag{11}$$

In this equation, D represents the diameter, H stands for the height, and μ_1 denotes the static shear modulus. The application of a preload, μ_0, causes a shift in the system's stiffness coefficient, k_0. Simultaneously, it induces changes in the intrinsic frequency of the system and the damping ratio, consequently leading to alterations in the recorded output amplitude.

4.2. A Study of the Impact Response of a Protection System without Preloading Volume. The numerical simulation results are presented in Figure 7, with T1 representing the relaxation time. To facilitate comparison with the response of the protection system when no preload is applied, a relaxation test is carried out under the same conditions. However, in this test, a relaxation time of 4 ms is used. T2 denotes the rising phase of the acceleration, while T3 represents the decreasing phase. T4 indicates the moment inside the chamber, while T5 marks the moment when the projectile exits the gun barrel.

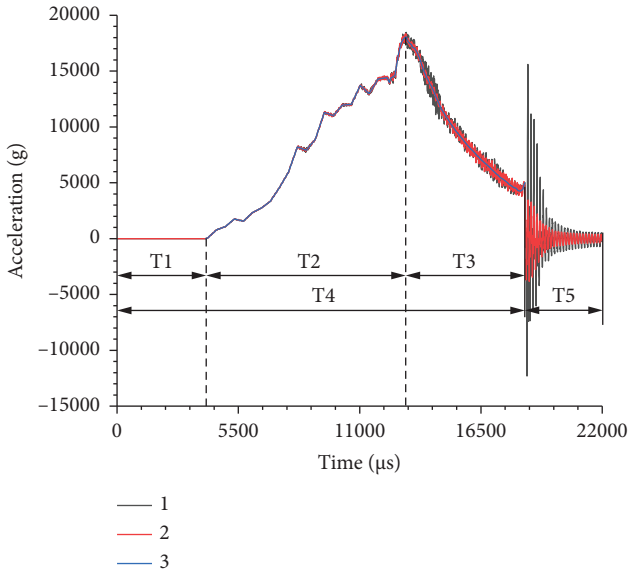

Figure 7: The curve of axial acceleration versus time without preload comprised three components: curve 1 depicted the axial acceleration versus time of the recorder, curve 2 illustrated the shell acceleration versus time, and curve 3 represented the loading curve.

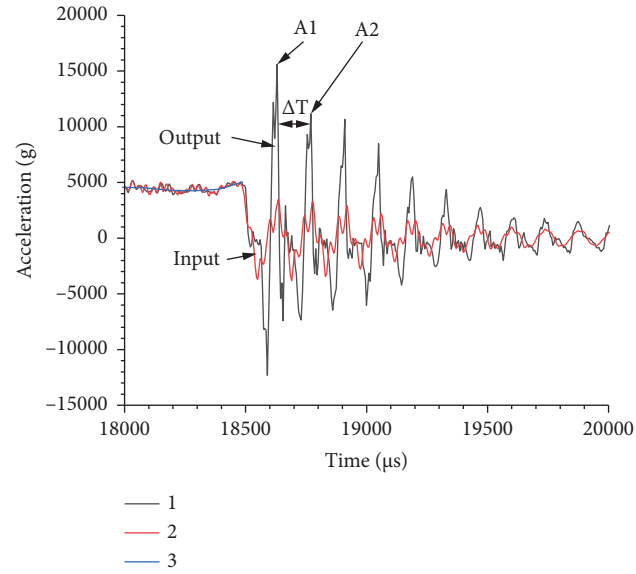

Figure 8: Acceleration of the projectile after exiting the muzzle as a function of time.

The analysis discloses that the loading curve, the recorder overload curve (curve 1), and the shell overload curve (curve 2) closely overlap during the T2 segment. Furthermore, it is observed that the shell exhibits slight oscillations and induces vibrations in the recorder during the T3 segment, with both amplitudes being in close proximity to each other.

After analyzing the acceleration curves of the shell and the recorder postmuzzle, it is evident that a substantial difference exists between the acceleration input from the shell and the peak acceleration recorded by the recorder. The maximum magnitude ratio reaches 4.5 : 1, indicating that the peak vibration experienced by the recorder is 4.5 times greater than the peak value of the shell input.

Furthermore, additional insights can be obtained from the response acceleration curve of the recorder. Specifically, it enables the calculation of the system's intrinsic frequency and damping ratio, as illustrated in Figure 8.

$$\frac{\omega_n}{2\pi} = \frac{\sqrt{k/m}}{2\pi} = \frac{1}{t_2 - t_1} = \frac{1}{18.769ms - 18.629ms} = 7.14kHz. \tag{12}$$

The logger weighs 0.046 kg:

$$\zeta = \frac{c}{2\sqrt{mp}} = \frac{\ln(A_1/A_2)}{2\pi} = \frac{\ln(15611/11165)}{2\pi} = 0.053. \tag{13}$$

The damping coefficient, $c = 218.75$ kg/s, is derived through analytical methods. With regard to the relationship between the stiffness coefficient and the level of precompression, a quasistatic stiffness coefficient is acquired:

$$k = k_0 = \frac{3\pi}{4}\frac{\mu_1 D^2 \mu_0}{(H-\mu_0)^2}\left[1 + \frac{D^2}{8H(H-\mu_0)}\right]. \tag{14}$$

Then, there is

$$\mu_1 = \frac{m(2\pi/t_2 - t_1)^2}{(3\pi)\left(D^2 H/(H-\mu_0)^2\right)\left[1 + (8H(H-\mu_0))\right]}. \tag{15}$$

With μ_0 set to 0, a value of μ_1 =15.0 MPa is obtained. The calculations indicate that the damping ratio and intrinsic frequency are influenced by the amount of preload applied. Figure 9 illustrates that as the preload increases, the frequency ratio (ω/ω_n) and the damping ratio decrease.

Given the fixed input frequency, an increase in preload, μ_0, leads to a decrease in the frequency ratio, ω/ω_n. This increase in preload, μ_0, results in a reduction of the acceleration amplitude (A_m) output to the recorder for the same frequency, ω. Additionally, the increase in preload, μ_0, causes a reduction in the damping ratio, further diminishing the acceleration amplitude (A_m) output to the recorder.

4.3. Effect of Preload on the Impact Response of a Protection System. While increasing the preload amount can enhance the stiffness of the outer protective material, it can also lead to higher compressive stress and structural deformation of the recorder, potentially causing damage. Therefore, it becomes imperative to conduct a comprehensive investigation into the structural forces acting on the recorder and the resulting acceleration (A_m) output under varying preload conditions.

4.3.1. Numerical Simulation Analysis of the Forces Acting on the Recorder due to Different Preload Amounts. The increase in preload amount results in a higher compression load on the recorder. Excessive preload has the potential to cause damage to the recorder. Hence, it is crucial to examine the forces exerted on the recorder under varying preload levels.

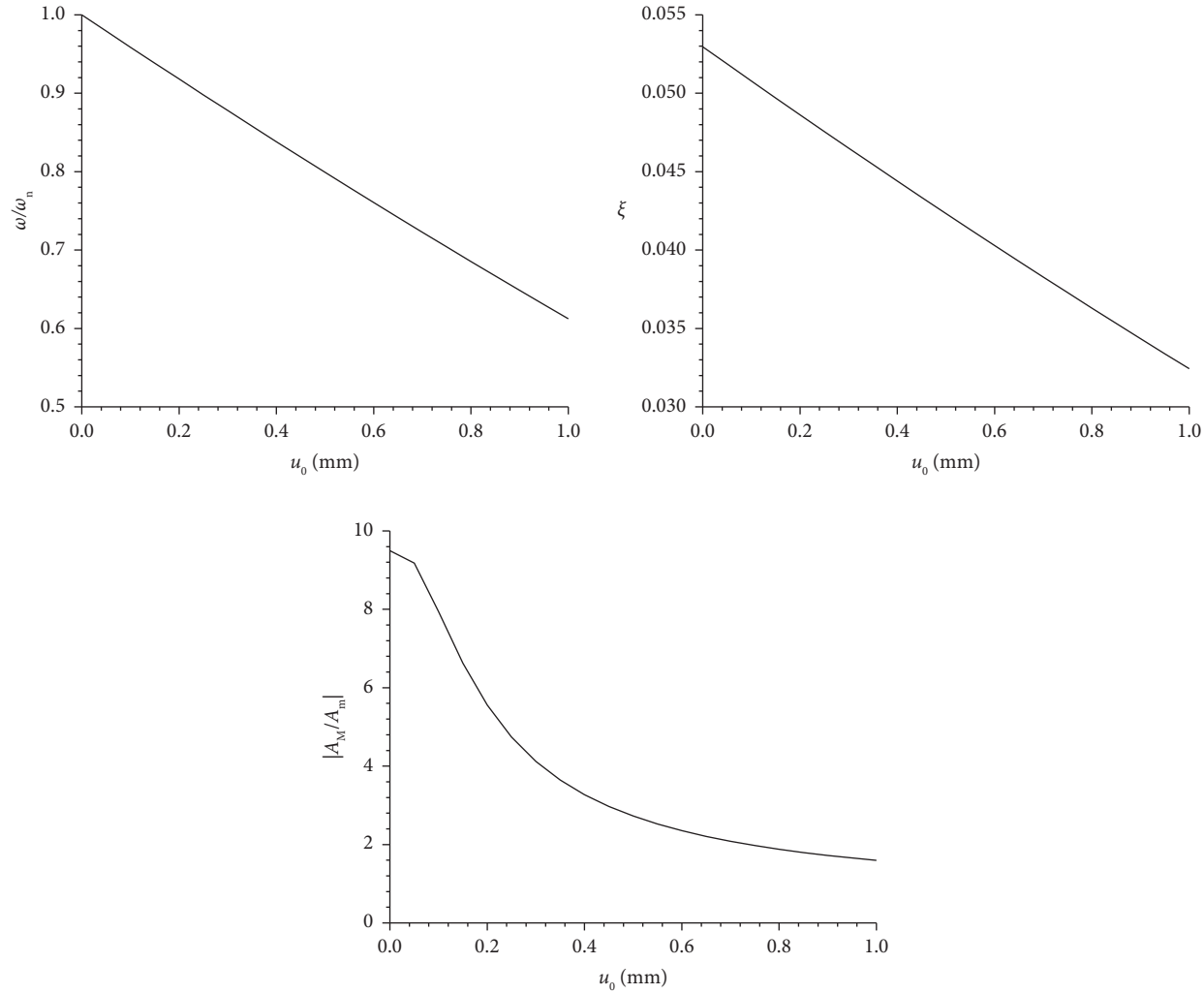

Figure 9: Frequency ratio and damping ratio with preload curve.

Figure 10 illustrates the stress distribution on the circuit board of the recorder when a preload of 0.2 mm is applied. An analysis reveals that, after the preload is applied, the two end surfaces of the circuit board experience significant stress, reaching 32.1 MPa, which is close to the circuit board's yield stress of 40 MPa. This significant stress load results in considerable deformation of the circuit board, especially in the outer layer with the epoxy resin potting material, potentially leading to the formation of microcracks.

As the shell's acceleration increases, the stress near the section where the acceleration is applied intensified. When the acceleration at the end face reached its peak, the stress at the bottom of the board surged to 43.2 MPa, surpassing the yield strength of the epoxy resin and causing plastic deformation. When the projectile exited the muzzle at 18.6 ms, the stress near the front end, close to the acceleration chip end, exceeded the stress at the bottom.

Figure 11 depicts the stress-time curve near the acceleration chip pin. An analysis revealed that with the initial preload applied, the stress near the pin initially increased rapidly with time, reaching 29.4 MPa, and then, it gradually rose to 37.9 MPa with the acceleration of the projectile. Such stress levels could lead to pin fracture. Additionally, stress near the acceleration chip pin oscillated after the projectile exited the muzzle. Thus, applying a significant preload could subject the acceleration chip to considerable stress during the projectile's acceleration phase, resulting in acceleration oscillations near the pin upon the projectile's exit from the muzzle. This, in turn, could result in cracks in the weld joints and pin detachment.

Upon analyzing the forward acceleration overload curve of the recorder in Figure 12, it is determined that the maximum acceleration recorded is 8786.5 g. This value is notably lower when compared to the peak acceleration of 15600 g observed in the absence of any preload. This indicates that the introduction of a 0.2 mm preload effectively reduced the peak acceleration experienced by the recorder.

Figure 13 illustrates the change in maximum stress near the acceleration sensor chip in response to alterations in preload volume. The analysis discloses that as the preload volume increased, the stress near the acceleration chip increased in an approximately linear fashion. Excessive stress levels had the potential to lead to chip damage. Hence, it is essential to exercise precise control over the preload volume to reduce the risk of circuitry damage during the preload application process.

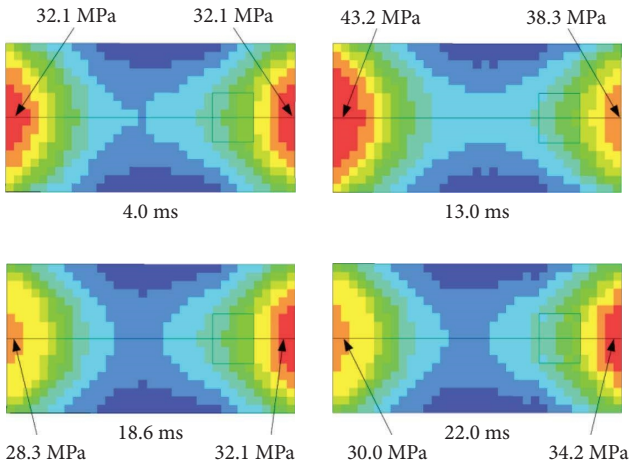

Figure 10: Von Mises stress distribution of the recorder board at different moments for a preload of 0.2 mm.

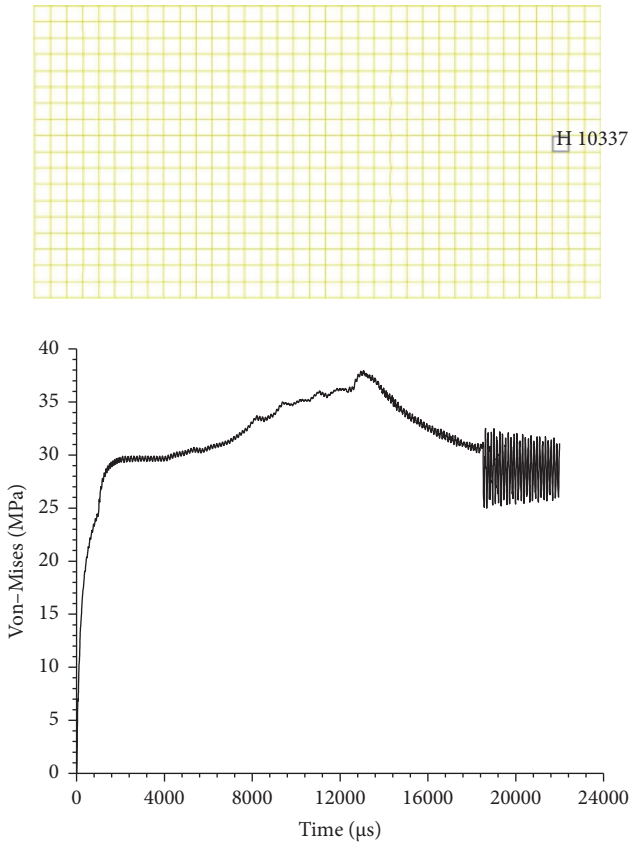

Figure 11: Stress versus time curve at accelerated chip pins.

4.3.2. Numerical Simulation Analysis of the Recorder's Vibration Amplitude under Various Preload Levels. Theoretical derivation reveals that increasing preload could decrease the intrinsic frequency of the spring damping system and increase the damping ratio, thereby reducing oscillation amplitude. However, it should be noted that an elevated preload also elevated the risk of circuit damage.

Figure 14 illustrates the influence of preload on the input and output functions of the acceleration amplitude ratio. The

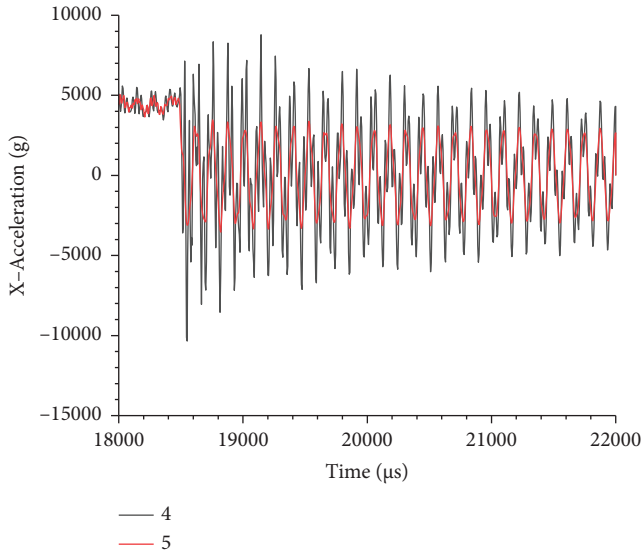

Figure 12: Acceleration curves of shell and recorder at 0.2 mm preload (1.8 ms~2.2 ms section, curve 4 is overload curve of recorder, and curve 5 is overload curve of shell).

analysis reveals that as the preload increased, both the maximum amplitude ratio of the input (shell) and the output (recorder) (a_m/a_M) gradually decreased. Notably, when the preload is set at 0.04 mm, the decrease in the maximum amplitude ratio of acceleration occurred at a slower rate.

Further analysis reveals that with respect to the input function, in the absence of preload, the shell's oscillation gradually diminishes over time, eventually stabilizing at a lower level of acceleration oscillation (450 g). However, in the presence of preload, the amplitude is higher compared to the scenario without preload.

Figure 15 illustrates the input function and output function change with preload variation. Upon examining the recorder's vibration, it is observed that even though the acceleration experienced by the recorder during the stable section is relatively lower in the absence of preload, a phase of vigorous vibration ensues after the projectile exits the gun's muzzle. This phase lasts for approximately 1.4 milliseconds and is characterized by substantial recorder oscillations in the absence of preload, subjecting it to higher overload shock. The amplitude of acceleration during this shock gradually decreases with an increase in preload amount. Without applying any preload, the peak acceleration at the gun's exit is measured at 15,611 g. However, when a preload of 0.04 mm is applied, the peak acceleration is significantly reduced to 7,080.9 g. This reduction in peak acceleration is substantial, amounting to a 54.6% decrease, highlighting the advantages of using a 0.04 mm preload.

5. Experimental Results and Discussion

Based on the analysis, it is determined that with a preload amount of 0.04 mm, the amplitude of acceleration output to the recorder when it exited the gun's muzzle is significantly reduced. Additionally, the compressive stress on the recorder due to this preload amount remains relatively low.

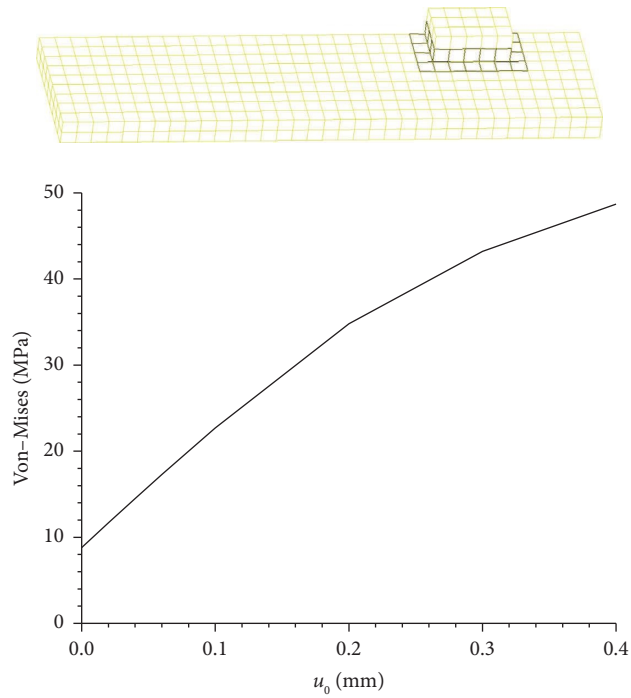

Figure 13: Maximum stress in the vicinity of the chip on the recorder board with different preloads.

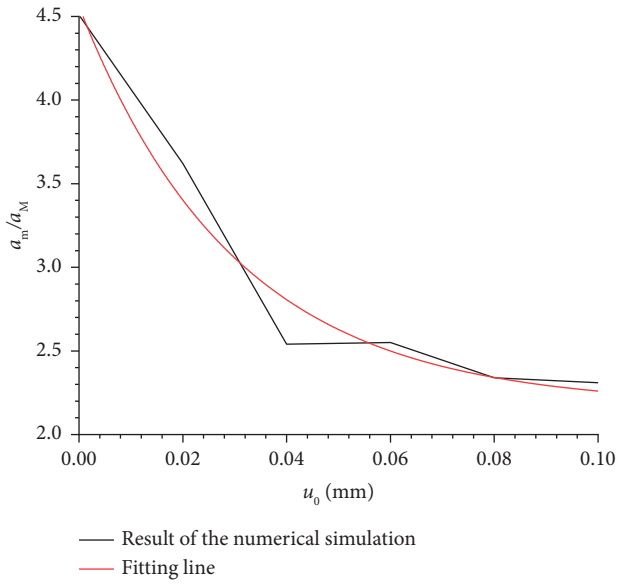

Figure 14: Input to output maximum magnitude ratio with preload curve.

This test effectively confirms the protection system's capability to withstand overloading and vibration. The ballistic recorder is launched from the gun and subsequently recovered at a considerable distance (500 m from the gun port) after traversing through sand and soil. After recovery, the data collected by the system are retrieved and analyzed. Figure 16 shows the test site layout.

After the recorder is recovered from the sandy soil and activated for testing, it undergoes disassembly. During this process, the memory chip on the circuit board is extracted to retrieve the data. Figure 17 presents both the structure of the disassembled recorder and the acceleration-versus-time curve retrieved from the memory chip. The time at the gun's exit serves as the starting point on the time axis.

Upon analyzing the test results, it is determined that the system can withstand high overloads (with a peak overload of 18074.2) and long pulse widths (overload duration of 14.5 ms) through the incorporation of a buffer layer between the projectile and the recorder, along with the application of a certain preload. The high-speed penetration of the soil by

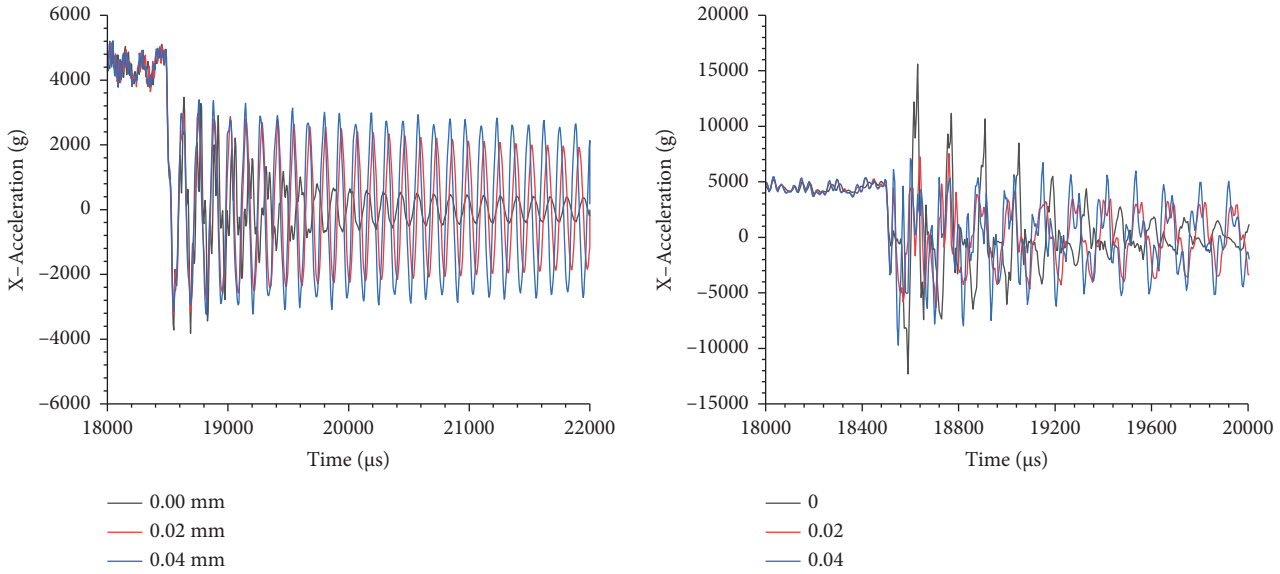

Figure 15: Input function and output function change with preload variation.

Figure 16: Test site layout.

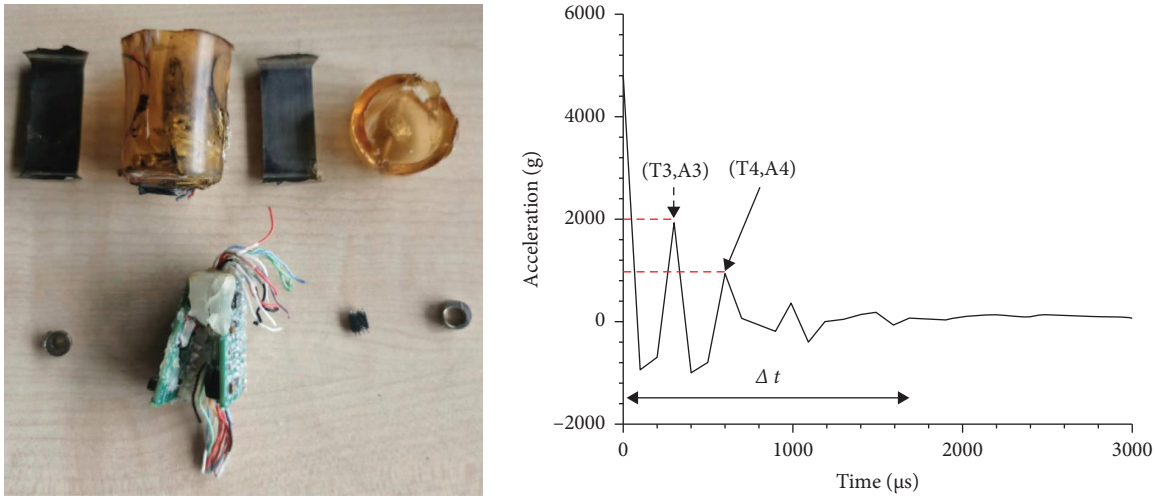

Figure 17: The disassembled logger and the data captured by the acceleration sensor.

the projectile, calculated as a muzzle velocity of 1235.1 m/s by integrating the acceleration overload curve before the muzzle exit, does not damage the recorder chip. This absence of damage demonstrates that the protective design structure makes the recorder highly resistant to vibrations and capable of withstanding high overloads.

Analyzing the results from the acceleration sensor data acquisition, it is observed that the amplitude attenuation ratio A3/A4 on the recorder is approximately 2.06, closely aligning with the numerical simulation results (A1/A2 = 1.93). However, the peak time difference T4-T3, recorded at 300 μs (frequency 3.3 kHz, given a recorder sampling rate of 20K), exceeds the numerical simulation results (140 μs). Test results further indicate that the time required for the acceleration to stabilize after exiting the muzzle is $\Delta t = 1.6$ ms, compared to the numerical simulation result of 1.4 ms. Additionally, the first peak acceleration after exiting the muzzle is 1917 g (while the muzzle acceleration is 5037.5 g), which is smaller in comparison to the numerical simulation results. These findings highlight that the polyurethane elastomer positioned between the projectile body and the recorder significantly reduces the projectile's vibration upon exiting the muzzle, thereby enhancing the system's ability to withstand high-frequency vibrations and overloads.

6. Conclusion

Utilizing theoretical analysis and numerical simulation calculations, this study investigates the impact of different preload levels on the vibration characteristics of the protective structure of a bullet-loaded recorder. Experimental validation is conducted to observe the changes in vibration acceleration within the recorder when preload is applied, resulting in the following conclusions:

Experimental findings demonstrate that employing a polyurethane elastomer for buffering between the projectile body and the recorder, along with the application of specific preload, enables the circuit system to withstand high overloads during launch, with a peak acceleration overload of 18,000 g and an overload duration of 14.5 ms. Moreover, it effectively dampens the high-frequency vibrations experienced by the projectile upon exiting the gun's muzzle, with a frequency of 3.3 KHz and an acceleration amplitude of 1,971 g.

Numerical simulations and theoretical calculations reveal that applying preload reduces the system's damping ratio and frequency ratio, consequently decreasing the output vibration acceleration amplitude, while the shell input remains constant. Numerical simulation results indicate that applying a 0.04 mm preload significantly reduced the vibration acceleration amplitude at the recorder compared to peak overload conditions without preload, achieving a 54.6% reduction.

The use of a polyurethane elastomer as a buffering material, along with a moderate preload, effectively suppresses the violent oscillations experienced by the projectile structure. This suppression results from reduced friction, gas expansion, and air resistance as the projectile approached the gun's muzzle. These measures play a crucial role in damping and safeguarding the recorder, offering valuable insights for research on bullet vibration protection. This study provides invaluable guidance for research on vibration damping and protection, especially in the context of ballistic projectiles [21–26].

Nomenclature

σ_y:	Yield stress
A:	The initial yield stress
B:	The strain-hardening modulus
n:	Hardening index
C:	Strain rate strengthening parameter
E:	Effective plastic strain
m:	Thermal softening parameter
p:	Pressure
C, S_1, S_2, and S_3:	The nondimensional coefficient
γ_0:	Gruneisen coefficient
γ_1:	First-order volume correction term
E:	Internal energy
σ_0:	Initial yield strength
E_h:	Hardening modulus
E:	Elastic model
E_t:	Tangent modulus
M:	Mass of the ballistic recorder protection system except for the recorder
m:	Mass of the recorder
a_M:	Acceleration of the ballistic recorder protection system
F_{1A} and F_{1B}:	Spring force
F_{2A} and F_{2A}:	Damping force $\dot{x}_M$ and $\dot{x}_m$ first-order partial derivative of the displacement
$\ddot{x}_M$ and $\ddot{x}_m$:	Second-order partial derivative of the displacement
c:	Damping coefficient.

Data Availability

The data used to support the findings of the study are included within the article.

Conflicts of Interest

The authors declare that they have no conflicts of interest.

References

[1] X. L. Chen, H. Zhao, M. Jiao, and H. F. Ye, "Dynamic response characteristics of the protection system for a projectile-borne recorder under high impact loading," *Explosion and Shock Waves*, vol. 39, no. 12, 2019.

[2] X. Xu, S. Q. Gao, S. H. Niu, L. Shen, S. H. Liu, and Z. C. Zhang, "Dynamic analysis of projectile-borne electronic devices under impact loading," *Acta Armamentarii*, vol. 38, no. 7, p. 1289, 2017.

[3] X. L. Chen, B. Liu, H. Zhang, and L. Liu, "Dynamic modelling and simulation for penetration warhead-fuze system," *Acta Armamentarii*, vol. 41, no. 4, p. 625, 2020.

[4] P. Verberne and S. A. Meguid, "Dynamics of precision-guided projectile launch: fluid-structure interaction," *Acta Mechanica*, vol. 232, no. 3, pp. 1147–1161, 2021.

[5] X. W. Yin, P. Verberne, and S. A. Meguid, "Multiphysics modelling of the coupled behaviour of precision-guided projectiles subjected to intense shock loads," *International Journal of Mechanics and Materials in Design*, vol. 10, no. 4, pp. 439–450, 2014.

[6] J. Wang, X. Xiao, Z. Deng, and M. Fu, "ISSA online estimation method for guided projectile angular rate based on magnetoresistive sensors," *IEEE Sensors Journal*, vol. 23, no. 1, pp. 256–264, 2023.

[7] P. Verberne, S. A. Meguid, and E. A. Elsayed, "Survivability of embedded microelectronics in precision guided projectiles: modeling and characterization," *International Journal of Impact Engineering*, vol. 154, Article ID 103864, 2021.

[8] L. H. Shu, L. He, Y. F. Wang, and C. G. Shuai, "Nonlinear mechanical model and character research on polyurethane isolator," *Journal of Vibration Engineering*, vol. 23, no. 5, pp. 530–536, 2010.

[9] Z. Q. Lu and L. Q. Chen, "Some recent progresses in nonlinear passive isolations of vibrations," *Chinese Journal of Theoretical and Applied Mechanics*, vol. 49, no. 3, pp. 550–564, 2017.

[10] M. Sjöberg and L. Kari, "Nonlinear isolator dynamics at finite deformations: an effective hyperelastic, fractional derivative, generalized friction model," *Nonlinear Dynamics*, vol. 33, no. 3, pp. 323–336, 2003.

[11] L. Kari, "The non-linear temperature dependent stiffness of precompressed rubber cylinders-An effective shape factor model," *Kautschuk Gummi Kunststoffe*, vol. 55, no. 3, pp. 76–81, 2002.

[12] J. Zhang and C. M. Richards, "Parameter identification of analytical and experimental rubber isolators represented by Maxwell models," *Mechanical Systems and Signal Processing*, vol. 21, no. 7, pp. 2814–2832, 2007.

[13] R. Rahnavard, H. D. Craveiro, and R. Napolitano, "Static and dynamic stability analysis of a steel-rubber isolator with rubber cores," *Structures*, vol. 26, pp. 441–455, 2020.

[14] C. M. Richards and R. Singh, "Characterization of rubber isolator nonlinearities in the context of single-and multi-degree-of-freedom experimental systems," *Journal of Sound and Vibration*, vol. 247, no. 5, pp. 807–834, 2001.

[15] C. Xueqian, S. Zhanpeng, H. Qinshu, D. Qiang, and L. Xin'en, "Influence of uncertainty and excitation amplitude on the vibration characteristics of rubber isolators," *Journal of Sound and Vibration*, vol. 377, pp. 216–225, 2016.

[16] G. R. Johnson and W. H. Cook, "Fracture characteristics of three metals subjected to various strains, strain rates, temperatures and pressures," *Engineering Fracture Mechanics*, vol. 21, no. 1, pp. 31–48, 1985.

[17] P. I. May and K. Formatn, *LS-DYNAkeyword User's Manual: Version 971*, Livermore Software Technology Corporation, Livermore, CA, USA, 2007.

[18] H. Wang, Y. Zhang, and J. Duan, "Experimental research on the mechanical properties of G50 alloy steel," *Acta Armamentarii*, vol. 30, no. 2, pp. 247–250, 2009.

[19] T. J. Holmquist, D. W. Templeton, and K. D. Bishnoi, "Constitutive modeling of aluminum nitride for large strain, high-strain rate, and high-pressure applications," *International Journal of Impact Engineering*, vol. 25, no. 3, pp. 211–231, 2001.

[20] X. Lin, X. Tong, Y. Chen, Z. Huang, and H. Yu, "The activity, distribution, and colocalization of cathepsin K and matrix metalloproteases in intact and eroded dentin," *Clinical Oral Investigations*, vol. 28, pp. 1–13, 2023.

[21] H. Zhang and X. F. Wang, "Optimization of isolated protection for the hard-target penetration fuze," *Journal of Vibration and Shock*, vol. 34, no. 24, pp. 92–196, 2015.

[22] X. M. Wang and W. B. Li, "Influence of multilayered media impedance matching on explosion interruption effect," *Journal of Vibration and Shock*, vol. 33, no. 17, pp. 105–110, 2014.

[23] Z. Q. Lv and L. H. Shu, "Shock mechanics model and characteristic analysis of polyurethane isolator with displacement restrictor," *Advanced Materials Research*, vol. 503-504, pp. 972–977, 2012.

[24] L. Jiang, X. Z. Zhang, L. M. Wang, L. Wu, and F. Y. Tian, "Nonlinear performance of a polyurethane isolator with large impact," in *Proceedings of the 22nd International Conference on Sound and Vibration*, pp. 12–16, Florence, Italy, June 2015.

[25] A. Gosar, I. Emri, J. Klemenc, M. Nagode, and S. Oman, "On the vibration-damping properties of the prestressed polyurethane granular material," *Polymers*, vol. 15, no. 5, p. 1299, 2023.

[26] N. R. Khatri and P. F. Egan, "Tailored energy absorption for 3D printed multi-material cellular structures using ABS and TPU," *ASME International Mechanical Engineering Congress and Exposition*, vol. 85680, 2021.